A dynamic spectrum of monocytes arising from the in situ reprogramming of CCR2+ monocytes at a site of sterile injury

Daniela Dal-Secco,[1]* Jing Wang,[1,2]* Zhutian Zeng,[1,2] Elzbieta Kolaczkowska,[1] Connie H.Y. Wong,[1] Björn Petri,[1,2] Richard M. Ransohoff,[4] Israel F. Charo,[5] Craig N. Jenne,[1,2]** and Paul Kubes[1,3]**

[1]Immunology Research Group, Snyder Institute for Chronic Diseases; [2]Department of Microbiology, Immunology, and Infectious Diseases; and [3]Department of Physiology and Pharmacology, University of Calgary, Calgary, Alberta T2N 4N1, Canada
[4]Neuroinflammation Research Center, Department of Neurosciences, Lerner Research Institute, Cleveland Clinic, Cleveland, OH 44195
[5]Gladstone Institute of Cardiovascular Disease and Cardiovascular Research Institute, Department of Medicine, University of California, San Francisco, San Francisco, CA 94143

Monocytes are recruited from the blood to sites of inflammation, where they contribute to wound healing and tissue repair. There are at least two subsets of monocytes: classical or proinflammatory (CCR2hiCX$_3$CR1low) and nonclassical, patrolling, or alternative (CCR2lowCX$_3$CR1hi) monocytes. Using spinning-disk confocal intravital microscopy and mice with fluorescent reporters for each of these subsets, we were able to track the dynamic spectrum of monocytes that enter a site of sterile hepatic injury in vivo. We observed that the CCR2hiCX$_3$CR1low monocytes were recruited early and persisted for at least 48 h, forming a ringlike structure around the injured area. These monocytes transitioned, in situ, from CCR2hiCx$_3$CR1low to CX$_3$CR1hiCCR2low within the ringlike structure and then entered the injury site. This phenotypic conversion was essential for optimal repair. These results demonstrate a local, cytokine driven reprogramming of classic, proinflammatory monocytes into nonclassical or alternative monocytes to facilitate proper wound-healing.

CORRESPONDENCE
Paul Kubes:
pkubes@ucalgary.ca
OR
Craig N. Jenne:
cnjenne@ucalgary.ca

Abbreviations used:
PI, propidium iodide;
RFP, red fluorescent protein;
SD-IVM, spinning-disk
intravital microscopy.

Effective responses to infection and injury have been directed by millions of years of evolutionary pressure. A response to sterile injury such as trauma has been optimized to include essential components of repair while excluding unwanted or disruptive influences. Understanding evolution-driven responses to sterile injury will be critical to understanding and modulating iatrogenic or lifestyle-driven inflammatory disease. The initial immune response to sterile traumatic injury, classically defined as tissue injury in the absence of infection, is most notably characterized by early neutrophil swarming into the site, a process that has been extensively studied and well documented, highlighting sequential phases of cellular recruitment (Chtanova et al., 2008; McDonald et al., 2010; Lämmermann et al., 2013).

Less is known about monocyte recruitment. Monocytes had been thought to enter at a delayed time point although this view has been challenged (Auffray et al., 2007). Moreover, monocytes have been demonstrated to possess impressive plasticity and have been implicated not only as proinflammatory but also as reparative cells (Geissmann et al., 2003; Gautier et al., 2012; Gordon, 2012). Literature to date suggests that they are endogenously present as at least two distinct populations: (1) as a classical proinflammatory cell circulating in blood and expressing high levels of CCR2 and Ly6C and low levels of CX$_3$CR1 (CCR2hiCX$_3$CR1low) and (2) as a locally patrolling alternative nonclassical monocyte with high levels of CX$_3$CR1
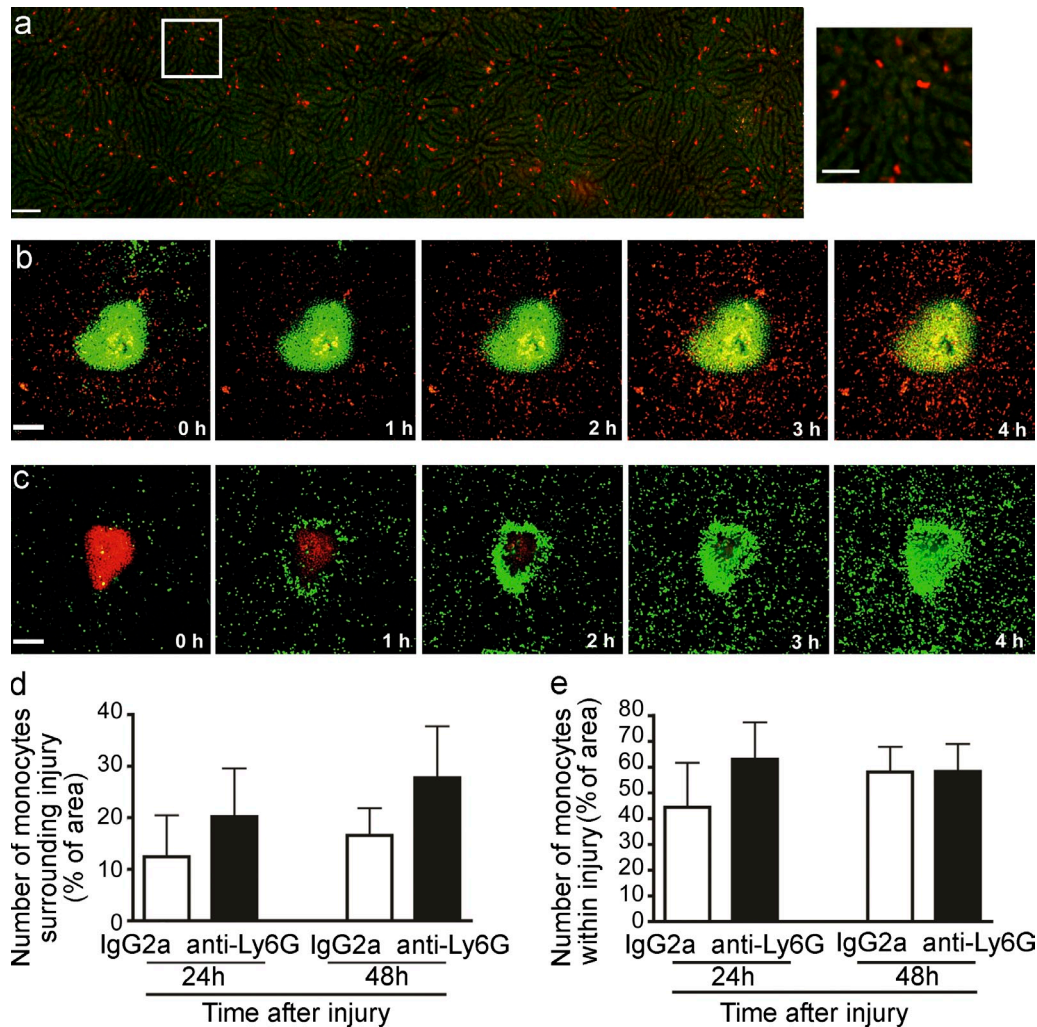
Figure 1. Neutrophils and monocytes traffic to site of hepatic sterile injury. (a, left) Mosaic of high-power images of CCR2+ cells in livers of *Ccr2^RFP/+* mice visualized by SD-IVM. Autofluorescent hepatocytes (green); RFP+ cells (red). Bar, 100 μm. (right) Magnification of area outlined in white. Bar, 50 μm. (b and c) Time lapse (0 to 4 h) images from a *Ccr2^RFP/+* (b) or a LysM-eGFP mouse (c) demonstrating the response of CCR2+ monocytes (red, b) or neutrophils (green, c) to focal hepatic injury (Sytox; green in b; propidium iodide; red in c). Bars, 200 μm. (d and e) Quantification of RFP+ monocytes (measured by % of area covered by RFP) either surrounding lesion (d) or within the lesion (e) following focal injury in *Ccr2^RFP/+* mice. Mice were pretreated with anti-Ly6G to deplete neutrophils or with Rat IgG2a as control. Error bars are the SEM. (d and e) Data are representative of at least four independent experiments.

and low or absent CCR2 ($CX_3CR1^{hi}CCR2^{low}$) and Ly6C (Geissmann et al., 2003; Sunderkötter et al., 2004). The $CCR2^{hi}CX_3CR1^{low}$ monocytes are believed to be selectively recruited to inflamed tissues and produce high levels of inflammatory cytokines during infection or tissue damage and may become tissue macrophages (Palframan et al., 2001; Geissmann et al., 2003; Sunderkötter et al., 2004; Varga et al., 2013; Hilgendorf et al., 2014), whereas the distinct $CX_3CR1^{hi}CCR2^{low}$ monocytes are thought to be primarily reparative, producing IL-10 in inflammatory milieus. They may become alternative macrophages (Arnold et al., 2007; Auffray et al., 2007).

We used spinning-disk fluorescent confocal intravital microscopy (SD-IVM) to track neutrophils and the two subsets of monocytes in an effort to examine their dynamic behavior in a bona fide sterile tissue injury. We have identified that only $CCR2^{hi}CX_3CR1^{low}$ monocytes are recruited to the injured liver followed by a cytokine-driven switch to $CCR2^{low}CX_3CR1^{hi}$ monocytes in the proximity of the lesion. This suggests local education and regulation of monocyte subtypes during the repair process.

RESULTS AND DISCUSSION

A tiny 0.02 ± 0.001 (SEM) mm³ sterile necrotic lesion was created in the liver with a thermal probe. Under basal conditions, no resident neutrophils were seen patrolling the liver vasculature and unlike other tissues, no nonclassical $CX_3CR1^{hi}CCR2^{low}$ monocytes were detected patrolling the liver sinusoids. Unexpectedly, the liver had a resident population of patrolling $CCR2^{hi}CX_3CR1^{low}$ cells (Fig. 1 a, left and right;
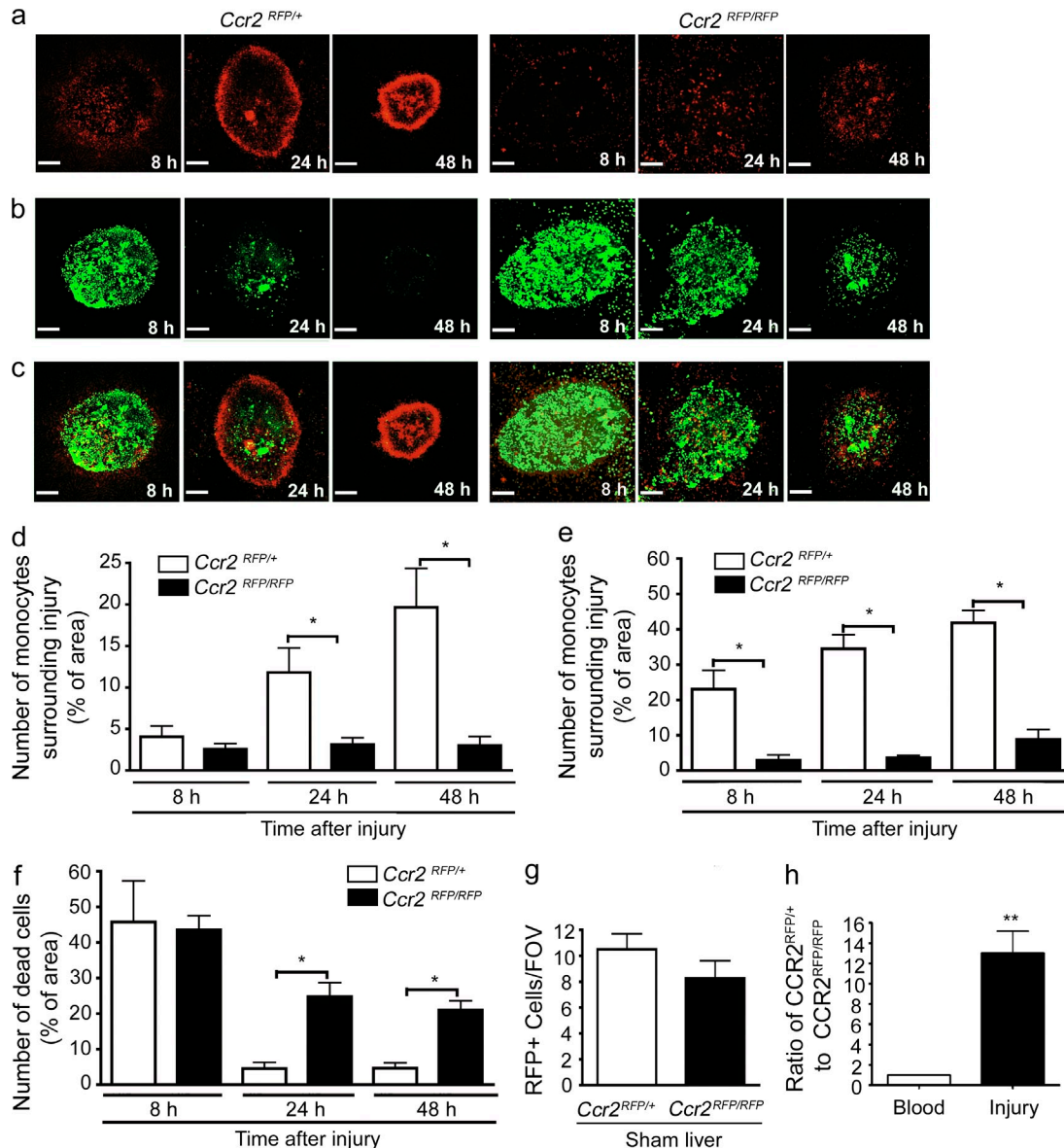
Figure 2. Proinflammatory monocytes home to site of sterile injury and facilitate tissue repair. (a–c) Images from 8 to 48 h after focal necrotic injury of the liver demonstrating the response of $Ccr2^{RFP/+}$ (left) and $Ccr2^{RFP/RFP}$ monocytes (right). (a) CCR2-RFP monocytes (red), (b) necrotic cells (green), (c) overlay. Bars, 200 µm. Data are representative of at least four independent experiments. (d and e) Quantification of RFP monocytes in $Ccr2^{RFP/+}$ and $Ccr2^{RFP/RFP}$ mice (measured by percentage of area covered by RFP) either surrounding lesion (d) or within the lesion (e). Data are representative of at least two independent experiments, each with three mice per group. (f) Quantification of dead cells (measured as percentage of area covered by Sytox green) within the lesion. (g) Quantification of monocytes per field of view (FOV) in the liver from sham-operated $Ccr2^{RFP/+}$ and $Ccr^{RFP/RFP}$ mice. (d–g) $n = 6$ mice per group; error bars are the SEM. (h) Monocytes were harvested from the bone marrow of Ccr2$^{RFP/+}$ and Ccr2$^{RFP/RFP}$ mice, mixed 1:1 and i.v. transferred to a WT recipient 6 h after focal injury. 24 h after transfer, the ratio of Ccr2$^{RFP/+}$:Ccr2$^{RFP/RFP}$ monocytes were measured in the blood and surrounding the liver injury. Data are representative of one experiment with three mice per group.

and Video 1) that crawled within the vasculature at velocities similar to those previously described for nonclassical CX_3CR1^{hi} CCR2^{low} monocytes (Auffray et al., 2007). However only ~5% of these cells appear to be classic monocytes as assessed by both CCR2 and Ly6C (unpublished data). The remaining RFP$^+$ cells were NK cells and some subsets of lymphocytes. Upon injury, the resident patrolling CCR2^{hi} CX_3CR1^{low} monocytes, not NK or T cells, begin to accumulate

around the injured area (Fig. 1 b and Video 2). At 8 h, some RFP$^+$ cells entered the injury site and persisted within the lesion for at least 48 h (Fig. 2 a, left). At 24 h, additional CCR2^{hi}CX$_3$CR1^{low} monocytes, were observed to encircle the injured area (Fig. 2, a, left, d) and collectively consolidated to fill the injury site from 48 h onward (Fig. 2, a and e). In contrast, hundreds of neutrophils crawled through the sinusoids to the focal necrosis as previously described (McDonald
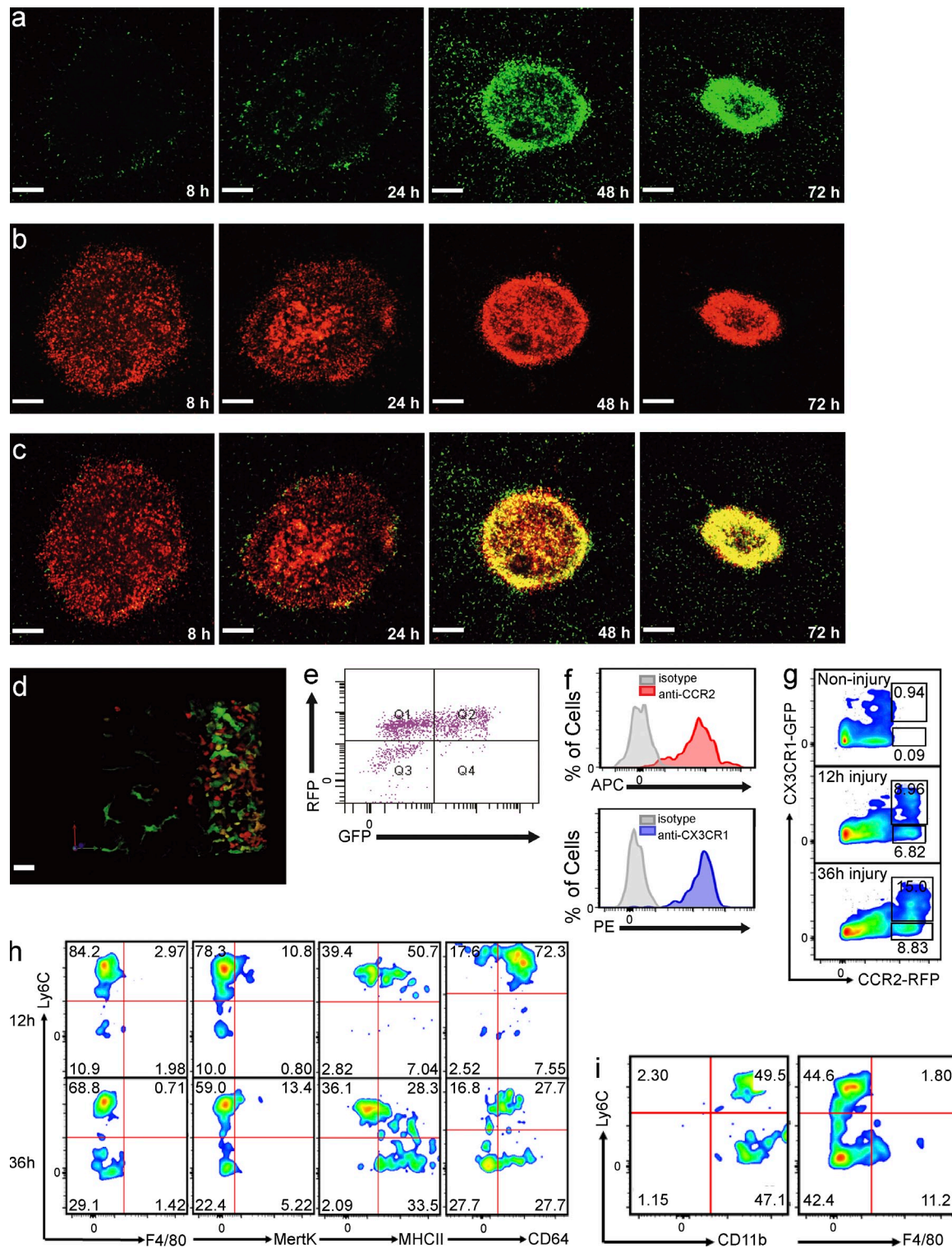
Figure 3. CCR2⁺CX₃CR1⁺ double–positive monocytes surround and enter the site of hepatic sterile injury. (a–c) Representative images taken 8 to 72 h after focal injury to the liver of *Ccr2^{RFP/+}/Cx3cr1^{GFP/+}* mice. (a) GFP, (b) RFP, and (c) overlay. Bars, 200 µm. (d) Extended focus image generated from a z-stack of the monocytic ring surrounding a focal injury in the liver of a *Ccr2^{RFP/+}/Cx3cr1^{GFP/+}* mouse demonstrating a spectrum of monocytes (red, orange, yellow, and green). (a–d) Images are representative of at least six independent experiments. (e) Representative FACS analysis of cells isolated from biopsy punches of the focal necrotic injury sites 48 h after injury, confirming the presence of a spectrum of monocytes. Pregated on size to exclude debris, viability, and CD11b⁺Ly6C⁺. (f) FACS analysis of cells obtained from the injury showing surface expression of CCR2 (top) and CX₃CR1 (lower). Cells pregated on size, viability, Ly6G⁻CD45⁺, and RFP⁺GFP⁺ followed by measurement of APC-conjugated

et al., 2010), completely infiltrating the injury within the first 3–4 h (Fig. 1 c). The differences in temporal recruitment and cell migration dynamics suggest that neutrophils and monocytes each have their own independent program of recruitment, a notion that was further supported by the observation that depletion of neutrophils had no impact on CCR2^{hi}CX$_3$CR1^{low} monocyte recruitment (Fig. 1, d and e) and interventions to prevent monocyte recruitment had no effect on neutrophil recruitment (discussed in detail below).

Once the ring was formed, many CCR2^{hi}CX$_3$CR1^{low} monocytes were seen meandering in and out of the ring in an apparently random pattern (Video 3). The CCR2 receptor was critical for this monocyte recruitment to the general area of the lesion, as CCR2-deficient (*Ccr2*$^{RFP/RFP}$) mice had a significant reduction in monocyte recruitment to the injury site (Fig. 2, a, right, e; and Video 4) and abolition of the ring formation at later time points (Fig. 2 d). CCR2 has been shown to be critical for mobilization of monocytes from bone marrow during systemic models of inflammation; however, these same studies have not noted a decrease in basal levels of monocytes or macrophages in tissues (Tsou et al., 2007; Engel et al., 2008). Our injury is tiny by comparison and may not require mobilization of monocytes from bone marrow. Moreover, the number of CCR2^{hi}CX$_3$CR1^{low} cells patrolling the liver vasculature under basal conditions was very similar in wild-type and *Ccr2*$^{RFP/RFP}$ mice (Fig. 2 g). Adoptive transfer of equal numbers of Ccr2$^{RFP/+}$ and Ccr2$^{RFP/RFP}$ monocytes demonstrates a failure of CCR2-deficient cells to accumulate at the injury site despite their abundance in the blood (Fig. 2 h).

We next investigated the clearance of necrotic debris in this model. Quantification of propidium iodide (PI) staining confirmed that necrotic cells were removed over a 48-h period. Labeling of necrotic cells with Sytox (Fig. 2b) was identical to PI but allowed for simultaneously imaging of CCR2$^+$ monocytes (red) relative to the necrotic debris area (green; Fig. 2 b). Fig. 2 c (left) clearly shows that as the dead cells condense into a smaller area, the surrounding monocytic ring also condenses. To determine whether the diminution of the injury site was causally related to the monocytic infiltrate we used *Ccr2*$^{RFP/RFP}$ mice and noted a significant delay in debris clearance over the first 48 h after injury (Fig. 2, b and c [right] and h) versus wild-type (Fig. 2, b and c [left] and f).

Cx3cr1$^{GFP/+}$ mice have revealed a population of resident monocytes that patrol the vasculature of tissues such as kidney and skin and are recruited very rapidly in infectious models of disease (Auffray et al., 2007; Carlin et al., 2013). These cells were not present in liver under basal conditions, although we did observe large cells with ramified structures, presumably

both dendritic cells and Ito cells. All of these *Cx3cr1*$^{GFP/+}$ cells were outside the sinusoids and their morphology was easily distinguishable from monocytes (Lee et al., 2010). Furthermore, very few infiltrating *Cx3cr1*$^{GFP/+}$ monocytes were seen at 8 h and only a very subtle ring of cells became visible at 24 h (Fig. 3 a). By 48 h, a clear ring of *Cx3cr1*$^{GFP/+}$ monocytes was noted (Fig. 3 a) and their distribution was identical to the ring formed by the *Ccr2*$^{RFP/+}$ monocytes (Fig. 2 a). Examination of the temporal relationship of the proinflammatory (CCR2^{hi}CX$_3$CR1^{low}) and alternative (CX$_3$CR1^{hi} CCR2^{low}) monocytes using the double reporter mouse, *Ccr2*$^{RFP/+}$/*Cx3cr1*$^{GFP/+}$, revealed that the CCR2^{hi} cells (red) arrived and stayed at the injury site between 8 and 72 h after injury (Fig. 3 b), whereas the CX$_3$CR1^{hi} (green) cells became prevalent at 48 and 72 h (Fig. 3 a) with identical localization to the CCR2^{hi} (red) cells. As shown in Fig. 3 c, there was a distinct yellow ring of monocytes at 48 h; this ring migrated into the injury site by 72 h. Because the ring was so densely packed with cells, it was difficult to determine whether the green cells were overlapping red cells (resulting in a yellow color) or whether there was a population of true yellow cells. Therefore, we used chimeric mice to dilute the ring with transgenic cells and observed, in a detailed 3-D reconstruction of the ring, that there was a very dynamic spectrum of cells ranging from red to orange to yellow to green cells (Fig. 3 d). It is worth noting that there were also some very large green cells which resemble the stellate or Ito cells (liver pericytes).

Clearly, the yellow ring was not simply a composition of overlapping distinct red or green monocytes but rather was made up of a spectrum of monocytes of varying hues (Fig. 3 d and Video 5). Interestingly, no green cells were ever seen infiltrating or crawling into the ring. This finding suggested the appearance of CX$_3$CR1$^+$ cells at the injury site resulted from an in situ switching of monocyte phenotypes from red to yellow to green within the cellular cluster surrounding injury site.

Harvests from multiple biopsies of injury sites confirmed not only the presence of CCR2$^+$ monocytes by flow cytometry but also a vast population of double-positive CX$_3$CR1$^+$CCR2$^+$ cells, suggesting a diverse spectrum of transitioning cells (Fig. 3 e). Only a few cells were exclusively green at this time point (Fig. 3 e). Because the RFP protein may have a longer half-life than membrane-associated CCR2 (perhaps CCR2 is internalized), we measured and report high levels of CCR2 on the CX$_3$CR1$^+$ monocytes (Fig. 3 f). Ly6C staining revealed a Ly6C^{high} signal early in the injury but a progressive reduction of Ly6C staining with time (Fig. 3, g and h). We explored other tissues, including the spleen and lung under

anti-CCR2 labeling (top) or pregated on size, viability, and Ly6G$^-$CD45$^+$, CCR2$^+$GFP$^+$, followed by measurement of PE-conjugated anti-CX$_3$CR1 labeling (lower). (g) FACS analysis of CCR2$^+$CX$_3$CR1$^+$ cells within the injury at the indicated time points. Cells pregated on size, viability, and Ly6G$^-$CD45$^+$. (h) FACS phenotyping of the CCR2$^+$CX$_3$CR1$^+$ cells 12 and 36 h after focal liver injury. Cells pregated on size, viability, and Ly6G$^-$CD45$^+$. (i) FACS analysis of cells obtained 72 h after injury showing CD11b, Ly6C, and F4/80 expression. Cells pregated on size, viability, and Ly6G$^-$CD45$^+$RFP$^+$GFP$^+$. All FACS data are representative of at least three independent experiments.

basal conditions, but the majority of cells were either CCR2^{hi} CX$_3$CR1^{low} or CX$_3$CR1^{high}CCR2^{low} monocytes with very few double–positive yellow cells. A population of double-positive monocytes could be detected in the bone marrow, where it has been postulated that CCR2^{hi}CX$_3$CR1^{low} monocytes return to and mature into CX$_3$CR1^{high}CCR2^{low} monocytes (Sunderkötter et al., 2004; Varol et al., 2007).

Biopsies of the injury at various time points allowed more complete characterization of the cell types and monocyte subpopulations. The RFP^{+} cells within the injury site were essentially all monocytes and not NK cells or lymphocytes. The monocytes showed a decrease in Ly6C between 12 and 36 h after injury but retained high levels of CD11b, MHC class II, and CD64 (Fig. 3 h). The cells were not transitioning directly into macrophage as neither F4/80 nor Mertk could be detected on their surface. Even at 72 h, F4/80 was still absent on the majority of the Ly6C^{lo} monocytes (Fig. 3 i).

To determine that observed yellow cells resulted from CCR2^{high}CX$_3$CR1^{low} (red) cells changing into intermediate double–positive cells, we established an ex vivo procedure whereby we maintained a liver biopsy in oxygenated RPMI medium. One can clearly see a progression from reddish yellow to more–yellow–less–red over just a brief 2 h after the biopsy harvest (Fig. 4, a and b; and Video 6). Because these biopsy explants were removed from the animal, the appearance of new cell phenotypes is independent of any new cells arriving at the site supporting an in situ phenotype switch was occurring. The transition in individual cells occurred rapidly but not in unison, converting at different times over 24 h. Because the cells often migrate throughout the ring, some cells disappear over the tracking period (Fig. 4, a and b).

If the red CCR2^{high}CX$_3$CR1^{low} monocytes transition to green CX$_3$CR1^{high}CCR2^{low} monocytes, then blocking recruitment of CCR2^{high} cells should prevent CX$_3$CR1^{high} cells from appearing at the injury site. Indeed, using CCR2-deficient mice on the dual reporter background (Ccr2[RFP/RFP]/Cx3cr1[GFP/+]) revealed complete inhibition of recruitment of not only the CCR2^{high}CX$_3$CR1^{low} (red) cells but also of CX$_3$CR1^{high}CCR2^{low} (green) monocytes and the spectrum of yellow cells at 8, 24, and 48 h after injury (Fig. 4 c). It is worth noting that the very large dendritic and stellate cells (green) were not affected by the CCR2 deficiency. A study has reported decreased alternative monocyte recruitment in CX$_3$CR1-deficient mice (Auffray et al., 2007); however, Cx3cr1[GFP/GFP]Ccr2[RFP/+] mice revealed no reduction in this spectrum of monocytes and no change in clearance of necrotic cells (Fig. 4, d–f).
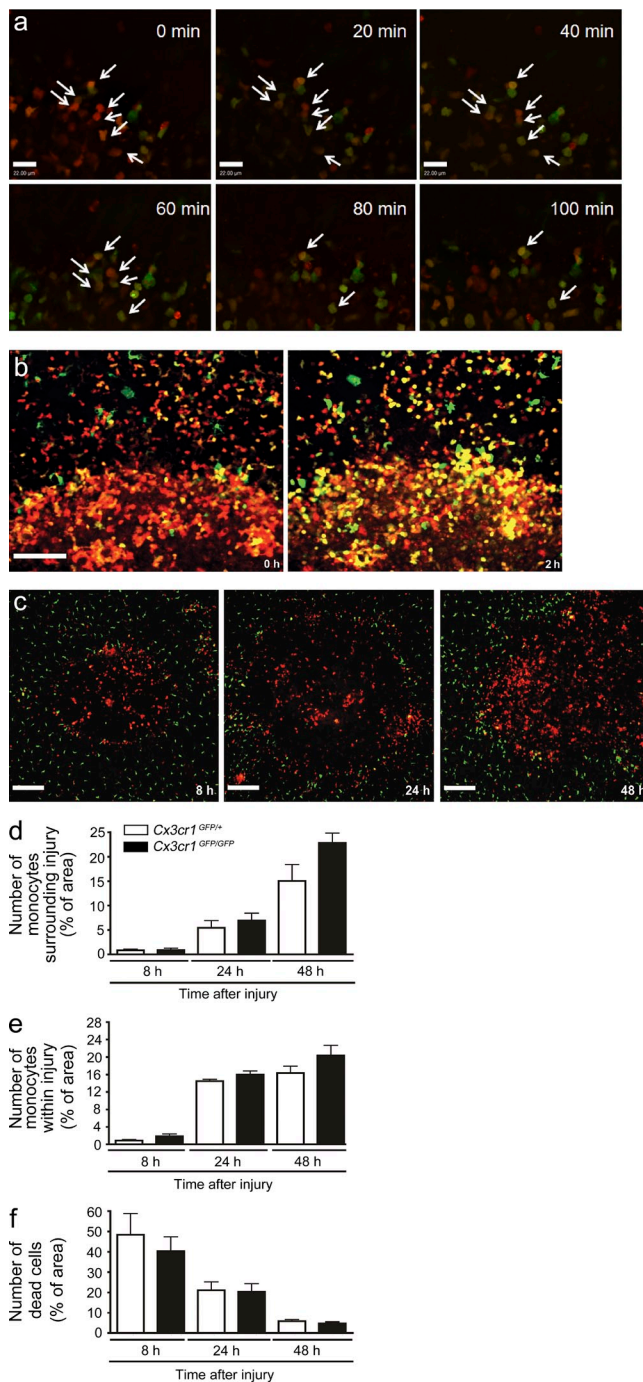
Figure 4.   Accumulation of reparative CX$_3$CR1^{+} monocytes at the site of sterile injury is independent of the CX$_3$CR1 receptor.
(a) A 2 mm × 1 mm biopsy punch of the sterile injury site was harvested from a Ccr2[RFP/+]/Cx3cr1[GFP/+] mouse 24 h after injury, maintained at 37°C, and 5% CO$_2$ and imaged. Time-lapsed images demonstrate a shift from red to green in individual cells (arrows). Bar, 22 μm. Data are representative of two independent experiments. (b) Image of the injury border immediately after tissue harvest (left) and again after 2 h of culture at 37°C and 5% CO$_2$ (right). Bar, 100 μm. Data representative of two independent experiments. (c) Representative images taken from 8 to 48 h after focal liver injury demonstrating failure to recruit Ccr2[RFP/RFP] cells to a site of injury

results in the lack of appearance of GFP^{+} cells in Ccr2[RFP/RFP]/Cx3cr1[GFP/+] mice. (d and e) Quantification of GFP monocytes in Cx3cr1[GFP/+] and Cx3cr1[GFP/GFP] mice (measured by percentage of area covered by GFP) either surrounding lesion (d) or within the lesion (e). (f) Quantification of dead cells (measured by percentage of area covered by Sytox orange) within the lesion. (d–f) n = 6 mice per group; error bars are the SEM.
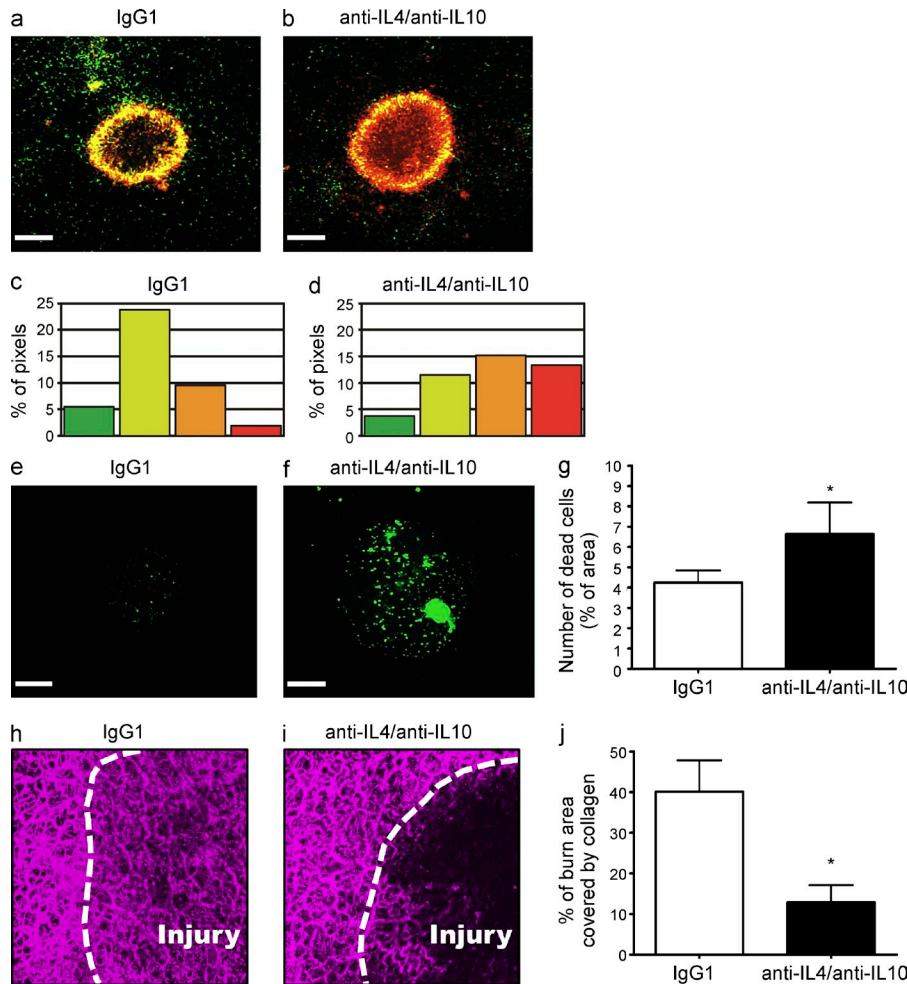
Figure 5. **CCR2+ monocytes transition into CCR2+CX$_3$CR1+ monocytes at a site of sterile injury in the liver.** (a and b) Conversion of RFP+ monocytes to RFP+GFP+ monocytes 48 h after focal liver injury in *Ccr2$^{RFP/+}$/Cx3cr1$^{GFP/+}$* mice (a) or *Ccr2$^{RFP/+}$/Cx3cr1$^{GFP/+}$* mice treated with anti–IL-4 and anti–IL-10-blocking antibodies (b). (c and d) Quantification of the percentage of each image corresponding to each of denoted hue in *Ccr2$^{RFP/+}$/Cx3cr1$^{GFP/+}$* mice (c) or *Ccr2$^{RFP/+}$/Cx3cr1$^{GFP/+}$* mice treated with anti–IL-4 and anti–IL-10 blocking antibodies (d). (e and f) Clearance of cellular debris 48 h after injury in control mice (e) and in anti–IL-4– and anti–IL-10–treated mice (f). (g) Quantification of dead cells (measured by percentage of area covered by Sytox green) within the lesion 48 h after injury. Bars, 200 µm; data are representative of three independent experiments. (h and i). Representative images of collagen in the liver of WT mice 72 h after focal injury. Mice treated with either an isotype control antibody (h) or anti–IL-4 and anti–IL-10-blocking antibodies (i). Injury border delineated with a dashed white line. (j) Quantification of collagen deposition within the burn 72 h after injury. Values expressed as a percentage of burn area covered by collagen. *n* > 3 mice per group; error bars, SEM. (h–j) Data representative of two independent experiments.

We hypothesized that monocyte reprogramming directly within the local environment was induced by cytokines. Numerous groups have suggested that IL-10 and IL-4 are important for transitioning from M1 to M2 macrophage. Indeed, the use of blocking antibodies revealed that inhibiting IL-10 and IL-4 in the local milieu delayed the transition from CCR2^{high}CX$_3$CR1^{low} to CX$_3$CR1^{high}CCR2^{low} monocytes (Fig. 5, a–d) suggesting that a similar program is important for monocyte conversion. Inhibition of IL-10 or IL-4 alone was insufficient to delay the transition. Importantly, clearance of necrotic material from within the lesion was also delayed when the monocytic switch was inhibited with anticytokine therapy (Fig. 5, e–g), suggesting that the progression from proinflammatory to alternative monocytes was fundamental to repair. Not only did preventing the monocytic switch delay debris clearance, but this failure to transition also inhibited collagen redeposition within the injury using two photon microscopy at 72 h after injury. Although collagen had been restored in mice treated with an isotype control antibody (Fig. 5 h), there was a significant delay in the process when IL-4 and IL-10 were inhibited (Fig. 5, i and j). A similar delay in collagen redeposition was observed in *Ccr2$^{RFP/RFP}$* mice at 72 h after injury (unpublished data).

Clearly, local reprogramming of monocytes can occur at the site of sterile injury and may allow for the local environment to drive conversion from proinflammatory to repair phenotype as is needed. This may be the most efficient way of locally regulating restitution in the liver. Adoptively transferred Ly6C^{high} monocytes could become a repair macrophage during fibrosis, although some have suggested that these cells may have migrated to bone marrow and matured into Ly6C^{low} monocytes before reaching the injury site (Sunderkötter et al., 2004). Use of SD-IVM and reporter mice for two lineages of monocytes has allowed us to track and delineate temporal and spatial events and reveal a transition from CCR2^{high}CX$_3$CR1^{low} to CX$_3$CR1^{high}CCR2^{low} monocytes within the tissue microenvironment surrounding a focal sterile injury. This transition was dependent on a local milieu of cytokines and independent of the recruitment of additional cells to the injury site. It is worth mentioning that other studies have argued against the conversion of Ly6C^{high} to Ly6C^{low} monocyte conversion in, for example, models of ischemic heart disease where sequential Ly6C^{high} followed by Ly6C^{low} monocyte recruitment was noted (Nahrendorf et al., 2007). Additionally, some studies have shown a transition from Ly6C^{high} monocytes to Ly6C^{low} F4/80+ macrophage in skeletal muscle (Varga et al., 2013; Hilgendorf et al., 2014).

Importantly, our data demonstrate a continuum of monocyte phenotypes rather than the two circumscribed profiles originally proposed. In this work, although only sterile injury was investigated in detail we do see similar responses in a preliminary series of data in an *S. aureus* model of liver infection. The responses to sterile injury and infection have been driven by millions of years of evolution and interestingly, both converge on a similar pathway. This convergence likely reflects an optimal immune and repair response. Our new understanding of monocyte plasticity within the tissue microenvironment could potentially open the door to novel targets of therapeutic intervention in cancer and other disease states.

MATERIALS AND METHODS

Mice. C57BL/6, LysM-eGFP (knock-in), and *Cx3cr1GFP/+* (knock-in) mice were obtained from The Jackson Laboratory. The generation of the *Ccr2RFP/+* (knock-in) mice have been described previously (Saederup et al., 2010). Animals were maintained in a specific pathogen–free facility at the University of Calgary Animal Resource Centre. All experiments involving animals were approved by the University of Calgary Animal Care Committee and were in compliance with guidelines established by the Canadian Council for Animal Care.

Antibodies and stains. Purified anti–mouse-Ly6G (clone 1A8), anti–mouse-IL-4 (clone 11B11), and anti–mouse-IL-10 (clone JES5-2A) were purchased from Bio X Cell; purified rat IgG2A (clone R35-95) and anti-CD16/CD32 (Fc block, clone 2.4G2) were purchased from BD. FITC-conjugated anti–mouse-CD31 (clone 390), PE-conjugated anti–mouse Ly6C (clone HK1.4), APC-eFluor-780 anti–mouse CD45 (clone 30-F11), eFluor-450-conjugated anti–mouse Ly6G (clone RB6-8C5), and eFluor-660–conjugated anti–mouse F4/80 (clone BM8) were purchased from eBioscience. FITC-conjugated rat anti–mouse CD11b (clone M1/70), PE-conjugated anti–mouse I-A/I-E (clone M5/114.15.2) and Alexa Fluor-647–conjugated anti–mouse CD64a/b (clone X54-5/7.1) antibodies were purchased from BD. APC-conjugated anti–mouse CCR2 (clone 47301) and APC-conjugated anti–mouse Mertk (clone 108928) antibodies were purchased from R&D Systems. PE-conjugated anti–mouse Cx₃CR1 (clone SA011F11) antibodies were purchased from BioLegend. Sytox Green, Sytox Orange (DNA dyes), and CellTracker Green CMFDA Dye were purchased from Invitrogen. Propidium iodide (PI) was purchased from Sigma-Aldrich.

Depleting and blocking antibody treatments. For neutrophil depletion, mice were administered either with 200 µg purified anti-Ly6G (1A8) or isotype control (IgG2a) i.p. 24 h and 1 h before injury induction and again 24 h after injury induction. For IL-4/IL-10 blocking experiments, mice were administered 500 µg purified anti–IL-4 together with 500 µg purified anti–IL-10, or they were administered 1 mg isotype control anti–mouse IgG1 i.p. at 12 and 24 h after injury induction.

Sterile inflammation induced by focal necrotic injury. Sterile inflammation induced by thermal injury in the liver was performed as described previously (McDonald et al., 2010). In brief, mice were anesthetized with isoflurane and a small incision was made just below the level of the diaphragm to expose the liver. A single focal injury was induced on surface of the liver to a depth of ∼80 µm using the tip of a heated 30-guage needle mounted on an electro-cautery device. In some experiments, necrotic cells were immediately labeled with a single application of 50 µl of 2.5 µM PI or 0.3 µM Sytox Green or Sytox Orange on the surface of the hepatic injury, followed by spinning-disk confocal intravital microscopy (SD-IVM). For other experiments, the incision was sutured closed and animals were allowed to recover for imaging of later time points (8–72 h) after injury. For sham experiments, animals underwent the same surgical procedure; however, no thermal injury was induced.

Preparation of the mouse liver for intravital microscopy. Intravital microscopy of the mouse liver was performed as previously described (Wong et al., 1997; Jenne et al., 2011). In brief, mice were anesthetized by i.p. injection of 200 mg/kg ketamine (Bayer Animal Health) and 10 mg/kg xylazine (Bimeda-MTC). After anesthesia, the right jugular vein was cannulated for maintenance of anesthetic and to permit the delivery of fluorescently labeled antibodies in certain experiments. Mouse body temperature was maintained on a special board thermostatically controlled at 37°C, with a transparent platform on which the hepatic tissue was placed. A midline incision followed by a lateral incision along the costal margin to the midaxillary line was performed to expose the liver. The mouse was place in a right lateral position and the ligaments attaching the liver to the diaphragm and the stomach were cut allowing the liver to be externalized onto a glass coverslip on the inverted microscope stage. Exposed abdominal tissues were covered with saline-soaked gauze to prevent dehydration. The liver was draped with a saline-soaked KimWipe and continuously superfused with physiological warm saline buffer to avoid tissue dehydration and to help restrict movement of the tissue on the slide. Exposed tissues were imaged by SD-IVM as described previously (Jenne et al., 2011). Typical laser power, exposure time and sensitivity settings are as follows; green channel (GFP⁺ cells, 80%, 455 ms, 199; Sytox Green, 80%, 343 ms, 88; Alexa Fluor-488 anti-CD31, 80%, 343 ms, 199), red channel (RFP⁺ cells, 80%, 455 ms, 199; Sytox Orange and PI, 80%, 343 ms, 88), far red channel (CD31–Alexa Fluor-647, 80%, 343 ms, 199).

3D model generation. Z-stacks of x–y planes (0.5-µm intervals) were imaged using an inverted spinning-disk confocal microscope or intravital multi-photon excitation microscope using either an ASI focus drive (Applied Scientific Instrumentation) or Olympus focus drive (Olympus). 3D isosurface models of monocytes or collagen in the liver were rendered within the Volocity software package (Improvision) using the 3D-opacity option. The same Black Level settings for each fluorescence channel were applied to all images. For 3D videos, individual frames were rendered using the default photobleaching compensation function within the Volocity software package.

Image processing. Images were exported from the Volocity acquisition software as TIF images and imported directly into the ImageJ software package V1.41 (National Institutes of Health) for analysis. Display items were processed using Photoshop (Adobe) to adjust the minimum threshold values for each of the fluorescence channels with the same threshold values being applied to images from all treatment groups within a single experiment. Videos underwent contrast enhancement within the Volocity software package, adjusting the Black Point for each fluorescence channel with the same settings being applied to the videos of all groups within a given experiment.

Semiquantitative analysis of monocytes and necrotic cells. Snapshots were generated from intravital videos and images corresponding to the red fluorescence channel alone (RFP⁺ cells; Sytox Orange or PI) or green fluorescence channel alone (GFP⁺ cells or Sytox Green) were exported for analysis in ImageJ. Image contrast was set to maximum to sharply define the borders of monocytes or dead cells. To account for variability in background fluorescence between experiments, and to eliminate fluorescence attributed to rapidly transiting monocytes, the minimum brightness threshold was adjusted for each single experiment with the same threshold being applied to all groups within a single experiment. Monocyte accumulation was then determined for each region (within the lesion or within a 100-µm-wide region surrounding the injury) and is expressed as percentage of the area labeled with either RFP (CCR2⁺ cells) or GFP (CX₃CR1⁺ cells). The necrotic area is expressed as percentage of the lesion stained with a cell death marker (Sytox Green, Sytox Orange, or PI).

Competitive recruitment of adoptively transferred monocytes. Bone marrow cells were harvested from *Ccr2RFP/+* and *Ccr2RFP/RFP* mice. Monocytes were isolated by monocyte isolation kit (Miltenyi Biotec). Flow cytometry confirmed >90% cells are Ly6C⁺ CD11b⁺ RFP⁺ after isolation.

Isolated CCR2$^{RFP/+}$ cells were labeled with CellTracker Green CMFDA (Life Technology), mixed 1:1 with CCR2$^{RFP/RFP}$ and i.v. transferred to a C57 recipient that had received focal liver injury 6 h before. 24 h after transfer, blood was collected and ratio of RFP$^+$CMFDA$^+$:RFP$^+$ was analyzed by FACS. Liver biopsy containing the injury was imaged by SD-IVM and the ratio of CCR2$^{RFP/+}$/CCR2$^{RFP/RFP}$ was determined by counting transferred cells within injury.

Determination monocyte hue. Hue analysis was performed using ImageJ. For each experiment, 4× images corresponding to the red and green fluorescence emission channels were merged into a RGB image (blue channel was blank). The image was segmented using the Color Threshold Tool using the brightness channel in the HSB (hue, saturation, and brightness) colorspace. Identical threshold levels were used for datasets acquired during the same imaging session. Pixels in the segmented region were classified according to hue (red, orange, yellow, and green). The relative percentage of pixels in each of the color classifications was then calculated.

Flow cytometry analysis. Mice were euthanized and liver biopsies of the injured area were collected into cold PBS. Single-cell suspensions were generated by mechanical disruption through a 40-μm nylon mesh, washed with cold PBS, resuspended in 40% isotonic Percoll (Sigma-Aldrich) and layered over 70% isotonic Percoll. Gradients were resolved through centrifugation for 25 min at 400 g in a bench-top centrifuge with no brake at room temperature, after which the interface containing the leukocytes was collected and washed in FACS wash buffer (FWB). Samples were blocked with anti-CD16/CD32 mAbs in FWB for 30 min at 4°C, followed by staining with fluorophore conjugated antibodies in FWB for 30 min at 4°C. The cells were washed in FWB, fixed in 1% formaldehyde, and analyzed on a LSRII (BD) or an Attune Acoustic Focusing Cytometer (Life Technologies). Figures were generated using either FlowJo (Tree Star), or Attune Cytometer software.

Ex vivo in situ conversion of monocyte phenotypes. 2 mm × 1 mm biopsy punches were harvested from the liver of *Ccr2$^{RFP/+}$/Cx3cr1$^{GFP/+}$* mice 24 h after the hepatic injury induction and maintained in RPMI medium without red phenol (Invitrogen) supplemented with 10% FBS and with L-glutamine biopsies at 37°C and 5% CO$_2$. Tissue explants were visualized by SD-IVM immediately after harvest and again every 20 min for 2 h.

Detection of hepatic collagen by multi-photon microscopy. The intravital multiphoton excitation microscopy presents nonlinear optical effects such as second-harmonic generation (SHG). This second-harmonic emission is able to envision collagen. In brief, intact or injured livers were removed, maintained in cold PBS, and imaged using a FV1000MPE multiphoton Olympus microscope equipped with a Chameleon Ultra laser Ti:Sapphire laser (Coherent) according to the procedure described previously (Petri et al., 2011). Hepatic tissue was visualized using a combination of multi-photon fluorescence and SHG using 890 nm excitation (Gailhouste et al., 2010). The signal was detected using an epi/backscattered geometry using nondescanned detectors and appropriate bandpass filters (GFP, 495–540 nm; RFP, 575–630 nm; SHG, 420–460 nm). Z-stacks were recorded at 0.5 μm intervals with a 20×/0.95 N.A. water dipping objective (Olympus).

Statistical analysis. All values were expressed as mean ± SEM. Data were compared either by unpaired two-tailed Student's t test or one-way ANOVA with Bonferroni multiple comparisons after hoc test. Statistical significance was accepted at P < 0.05.

Online supplemental material. Video 1 shows patrolling of the liver vasculature by CCR2$^+$ monocytes under basal conditions. Video 2 shows the early monocyte response to focal sterile injury in the liver. Video 3 shows the behavior of CCR2$^+$ monocytes around the site of a focal necrotic injury in the liver. Video 4 shows how CCR2-deficeint monocytes fail to accumulate at the site of focal necrotic injury in the liver. Video 5 highlights the spectrum of monocytes that surround a focal sterile injury of the liver. Video 6

is time-lapsed imaging demonstrating the in situ phenotype conversion of monocytes recruited to a site of injury. Online supplemental material is available at http://www.jem.org/cgi/content/full/jem.20141539/DC1.

REFERENCES

Arnold, L., A. Henry, F. Poron, Y. Baba-Amer, N. van Rooijen, A. Plonquet, R.K. Gherardi, and B. Chazaud. 2007. Inflammatory monocytes recruited after skeletal muscle injury switch into antiinflammatory macrophages to support myogenesis. *J. Exp. Med.* 204:1057–1069. http://dx.doi.org/10.1084/jem.20070075

Auffray, C., D. Fogg, M. Garfa, G. Elain, O. Join-Lambert, S. Kayal, S. Sarnacki, A. Cumano, G. Lauvau, and F. Geissmann. 2007. Monitoring of blood vessels and tissues by a population of monocytes with patrolling behavior. *Science.* 317:666–670. http://dx.doi.org/10.1126/science.1142883

Carlin, L.M., E.G. Stamatiades, C. Auffray, R.N. Hanna, L. Glover, G. Vizcay-Barrena, C.C. Hedrick, H.T. Cook, S. Diebold, and F. Geissmann. 2013. Nr4a1-dependent Ly6C(low) monocytes monitor endothelial cells and orchestrate their disposal. *Cell.* 153:362–375. http://dx.doi.org/10.1016/j.cell.2013.03.010

Chtanova, T., M. Schaeffer, S.J. Han, G.G. van Dooren, M. Nollmann, P. Herzmark, S.W. Chan, H. Satija, K. Camfield, H. Aaron, et al. 2008. Dynamics of neutrophil migration in lymph nodes during infection. *Immunity.* 29:487–496. http://dx.doi.org/10.1016/j.immuni.2008.07.012

Engel, D.R., J. Maurer, A.P. Tittel, C. Weisheit, T. Cavlar, B. Schumak, A. Limmer, N. van Rooijen, C. Trautwein, F. Tacke, and C. Kurts. 2008. CCR2 mediates homeostatic and inflammatory release of Gr1(high) monocytes from the bone marrow, but is dispensable for bladder infiltration in bacterial urinary tract infection. *J. Immunol.* 181:5579–5586. http://dx.doi.org/10.4049/jimmunol.181.8.5579

Gailhouste, L., Y. Le Grand, C. Odin, D. Guyader, B. Turlin, F. Ezan, Y. Désille, T. Guilbert, A. Bessard, C. Frémin, et al. 2010. Fibrillar collagen scoring by second harmonic microscopy: a new tool in the assessment of liver fibrosis. *J. Hepatol.* 52:398–406. http://dx.doi.org/10.1016/j.jhep.2009.12.009

Gautier, E.L., T. Shay, J. Miller, M. Greter, C. Jakubzick, S. Ivanov, J. Helft, A. Chow, K.G. Elpek, S. Gordonov, et al. Immunological Genome Consortium. 2012. Gene-expression profiles and transcriptional regulatory pathways that underlie the identity and diversity of mouse tissue macrophages. *Nat. Immunol.* 13:1118–1128. http://dx.doi.org/10.1038/ni.2419

Geissmann, F., S. Jung, and D.R. Littman. 2003. Blood monocytes consist of two principal subsets with distinct migratory properties. *Immunity.* 19:71–82. http://dx.doi.org/10.1016/S1074-7613(03)00174-2

Gordon, S. 2012. Targeting a monocyte subset to reduce inflammation. *Circ. Res.* 110:1546–1548. http://dx.doi.org/10.1161/RES.0b013e31825ec26d

Hilgendorf, I., L.M. Gerhardt, T.C. Tan, C. Winter, T.A. Holderried, B.G. Chousterman, Y. Iwamoto, R. Liao, A. Zirlik, M. Scherer-Crosbie, et al. 2014. Ly-6Chigh monocytes depend on Nr4a1 to balance both inflammatory and reparative phases in the infarcted myocardium. *Circ. Res.* 114:1611–1622. http://dx.doi.org/10.1161/CIRCRESAHA.114.303204

Jenne, C.N., C.H. Wong, B. Petri, and P. Kubes. 2011. The use of spinning-disk confocal microscopy for the intravital analysis of platelet dynamics in response to systemic and local inflammation. *PLoS ONE.* 6:e25109. http://dx.doi.org/10.1371/journal.pone.0025109

Lämmermann, T., P.V. Afonso, B.R. Angermann, J.M. Wang, W. Kastenmüller, C.A. Parent, and R.N. Germain. 2013. Neutrophil swarms require LTB4 and integrins at sites of cell death in vivo. *Nature.* 498:371–375. http://dx.doi.org/10.1038/nature12175

Lee, W.Y., T.J. Moriarty, C.H. Wong, H. Zhou, R.M. Strieter, N. van Rooijen, G. Chaconas, and P. Kubes. 2010. An intravascular immune response to Borrelia burgdorferi involves Kupffer cells and iNKT cells. *Nat. Immunol.* 11:295–302. http://dx.doi.org/10.1038/ni.1855

McDonald, B., K. Pittman, G.B. Menezes, S.A. Hirota, I. Slaba, C.C. Waterhouse, P.L. Beck, D.A. Muruve, and P. Kubes. 2010. Intravascular danger signals guide neutrophils to sites of sterile inflammation. *Science.* 330:362–366. http://dx.doi.org/10.1126/science.1195491

Nahrendorf, M., F.K. Swirski, E. Aikawa, L. Stangenberg, T. Wurdinger, J.L. Figueiredo, P. Libby, R. Weissleder, and M.J. Pittet. 2007. The healing myocardium sequentially mobilizes two monocyte subsets with divergent and complementary functions. *J. Exp. Med.* 204:3037–3047. http://dx.doi.org/10.1084/jem.20070885

Palframan, R.T., S. Jung, G. Cheng, W. Weninger, Y. Luo, M. Dorf, D.R. Littman, B.J. Rollins, H. Zweerink, A. Rot, and U.H. von Andrian. 2001. Inflammatory chemokine transport and presentation in HEV: a remote control mechanism for monocyte recruitment to lymph nodes in inflamed tissues. *J. Exp. Med.* 194:1361–1373. http://dx.doi.org/10.1084/jem.194.9.1361

Petri, B., J. Kaur, E.M. Long, H. Li, S.A. Parsons, S. Butz, M. Phillipson, D. Vestweber, K.D. Patel, S.M. Robbins, and P. Kubes. 2011. Endothelial LSP1 is involved in endothelial dome formation, minimizing vascular permeability changes during neutrophil transmigration in vivo. *Blood.* 117:942–952. http://dx.doi.org/10.1182/blood-2010-02-270561

Saederup, N., A.E. Cardona, K. Croft, M. Mizutani, A.C. Cotleur, C.L. Tsou, R.M. Ransohoff, and I.F. Charo. 2010. Selective chemokine receptor usage by central nervous system myeloid cells in CCR2-red fluorescent protein knock-in mice. *PLoS ONE.* 5:e13693. http://dx.doi.org/10.1371/journal.pone.0013693

Sunderkötter, C., T. Nikolic, M.J. Dillon, N. Van Rooijen, M. Stehling, D.A. Drevets, and P.J. Leenen. 2004. Subpopulations of mouse blood monocytes differ in maturation stage and inflammatory response. *J. Immunol.* 172:4410–4417. http://dx.doi.org/10.4049/jimmunol.172.7.4410

Tsou, C.L., W. Peters, Y. Si, S. Slaymaker, A.M. Aslanian, S.P. Weisberg, M. Mack, and I.F. Charo. 2007. Critical roles for CCR2 and MCP-3 in monocyte mobilization from bone marrow and recruitment to inflammatory sites. *J. Clin. Invest.* 117:902–909. http://dx.doi.org/10.1172/JCI29919

Varga, T., R. Mounier, P. Gogolak, S. Poliska, B. Chazaud, and L. Nagy. 2013. Tissue LyC6- macrophages are generated in the absence of circulating LyC6- monocytes and Nur77 in a model of muscle regeneration. *J. Immunol.* 191:5695–5701. http://dx.doi.org/10.4049/jimmunol.1301445

Varol, C., L. Landsman, D.K. Fogg, L. Greenshtein, B. Gildor, R. Margalit, V. Kalchenko, F. Geissmann, and S. Jung. 2007. Monocytes give rise to mucosal, but not splenic, conventional dendritic cells. *J. Exp. Med.* 204:171–180. http://dx.doi.org/10.1084/jem.20061011

Wong, J., B. Johnston, S.S. Lee, D.C. Bullard, C.W. Smith, A.L. Beaudet, and P. Kubes. 1997. A minimal role for selectins in the recruitment of leukocytes into the inflamed liver microvasculature. *J. Clin. Invest.* 99:2782–2790. http://dx.doi.org/10.1172/JCI119468